A Holographic Broadband Achromatic Metalens

Xinghao Wang, Shunli Liu, Liqun Xu, Yang Cao, Yuan Tao, Yiyu Chen, Zihang Zhang, Chao Chen, Jiawen Li, Yanlei Hu, Jiaru Chu, Dong Wu, Chaowei Wang,* and Jincheng Ni*

Metalens with nanostructured optical elements are designed to control wavefront shaping at the wavelength-scale thickness. However, most metalens still suffer from large chromatic aberrations due to phase dispersion, limiting their wide applications for multiple wavelengths. Here, avoiding complex resonant designs or multiple-layer nanostructures, a simple broadband achromatic metalens by holographic diffraction in the visible spectrum is demonstrated. The hyperbolic phase distributions of multiple discrete wavelengths within a shared aperture and fabricate a broadband achromatic diffractive metalens by flexible direct-laser-writing technique is randomly interleaved. The designed polarization-insensitive metalens modulate the light field by changing the height of the artificial neuron phase units to achieve average focusing efficiencies of 55% in the visible spectrum. This holographic design concept can pave the way to expand achromatic metalenses to multiple spectra.

1. Introduction

Optical lenses, indispensable components in optical systems, are typically limited by the chromatic aberration caused by the dispersion for wide bandwidths.[1,2] In terms of traditional refractive imaging lenses, the spatial distribution of the constructed dielectric material refractive index determines the deflection of the incident light. Since the refractive index of the dielectric material is related to the wavelength, the behavior of focus inevitably shows "positive dispersion." Generally, the method of reducing chromatic aberration is distinct dispersion complementation, including the achromatic doublet (triplet) of different glass-based materials[3,4] and the hybrid diffractive–refractive achromatic lens.[5–7] However, the multi-component design consequently makes the optical device bulky and heavy, which is

X. Wang, S. Liu, L. Xu, Y. Cao, Y. Tao, Y. Chen, Z. Zhang, J. Li, Y. Hu, J. Chu, D. Wu, C. Wang, J. Ni
CAS Key Laboratory of Mechanical Behavior and Design of Materials,
Department of Precision Machinery and Precision Instrumentation
University of Science and Technology of China
Hefei 230027, China
E-mail: chaoweiw@ustc.edu.cn; njc@ustc.edu.cn
C. Chen
Department of Materials Physics and New Energy Device
School of Materials Science and Engineering
Hefei University of Technology
Hefei 230009, China

in contrast to the trend toward miniaturization of modern optical systems. In addition, the misalignment between different devices in manufacturing seriously affects the performance of integrated optics.[8]

Metalens, a new class of planar optics lens, reshapes electromagnetic waves by using artificial subwavelength meta-atoms,[9–11] providing a compact design platform for functional lenses.[12–17] Very recently, the chromatic aberration of metalenses has been successfully tackled by customizing waveguide-like resonant modes,[18,19] and calculating the group delay.[20,21] Nevertheless, their practical wide applications are still limited mainly due to the relatively low efficiency and polarization sensitivity.[22] Although it is possible to improve the efficiency of metalens by using silicon and low-loss dielectric materials,[23,24] complex meta-atoms are highly required for manufacturing, such as high aspect ratio etching and multi-step operation.[25,26] Meanwhile, polarization insensitivity can be achieved by using cylindrical meta-atoms and inverse design.[27,28] However, it often has low focusing efficiency and is limited by intrinsic material loss above the bandgap, which is difficult to extend to multispectral windows.[21] Intriguingly, holographic metasurfaces can flexibly control complex light fields with high precision,[29,30] and have been extensively implemented in dispersive engineering such as spectrometers[14] and full-color display.[31–33] Moreover, holography has the characteristic of redundancy, showing almost perfect reconstructed optical fields by fragments of holograms. In principle, holography is possible to make a hologram for any operating spectral range.

Three-dimensional (3D) two-photon nanolithography is an important technology for the manufacturing of 3D structures,[34–36] which allows fast and flexible fabrication of micro- and nano-optical elements at nearly 100 nm resolution,[37,38] even complex multilayer broadband diffraction optical elements[39,40] and high aspect-ratio holographic elements.[41] In addition, the throughput of two-photon lithography can be significantly improved by adopting the multifocal strategy[42,43] and varying focusing conditions.[44] Thus, 3D two-photon nanolithography can fabricate meta-atoms of any shape flexibly and efficiently and makes the stacking of multiple layers easy. More importantly, polymer-friendly 3D two-photon nanolithography avoids the intrinsic optical loss in the constituent materials of metalenses, which is considered to be the key factor hindering metalenses from working on multiple spectral ranges. Recently, 3D-printed achromatic
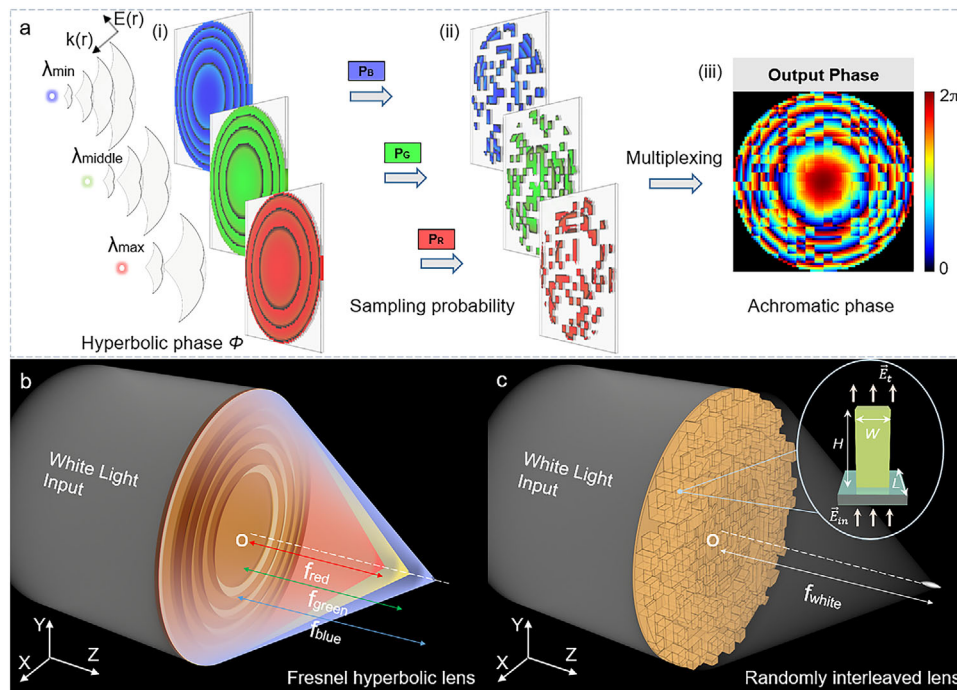
Figure 1. Concept of the randomly interleaved holographic broadband diffractive metalens. a) The process of random sampling and multiplexing of the hyperbolic phase in the diffractive plane. We can think of the abovementioned three wavelengths as discrete RGB channels whose control allows one to change the chromaticity in an optical system. p_B, p_G, and p_R are the probabilities of selecting the hyperbolic phase of each wavelength. b) Focusing performance of traditional Fresnel diffractive lens under white light irradiation. Focus dispersion shows negative dispersion characteristics. c) Focusing performance of the randomly interleaved broadband diffractive lens under white light irradiation. Through the spatial multiplexing scheme, an apochromatic diffractive metalens is designed to maintain the same focal length for several discrete wavelengths. Inset shows the schematic diagram of the artificial neuron phase unit, where $\vec{E}_{in}$ is the incident light field, and $\vec{E}_t$ is the transmitted light field.

metalenses, exploiting the height as another degree of freedom, have been successfully applied to near-infrared operation.[45–47] However, these works are subject to the principle of design and polarization conversion efficiency, and do not exhibit high-efficiency achromatic performance in the visible spectrum. A low-cost and universal holographic design method for achromatic 3D-printed metalenses that is insensitive to polarized light and has high efficiency remains unseen in the visible spectrum.

Here, we propose a holographic broadband diffractive metalens by randomly interleaved artificial neuron phase units.[48] By randomly interleaving hyperbolic phases of multiple distinct wavelengths, the point spread function (PSF) of the diffractive lens is balanced at multiple wavelengths within a single shared aperture without reducing the numerical aperture of each subelement.[49,50] In contrast to most metalenses, the randomly interleaved lens (RIL) can be fabricated in low refractive index materials, which provides advantageous access to free-form structures using femtosecond direct laser writing instead of multilevel or grayscale lithography and etching processes. Hence, relaxing feature height constraints (height of RIL ≈1.5 μm) provides additional degrees of freedom such that RIL can simultaneously reduce chromatic aberration (bandwidth ≈210 nm), improve focusing efficiency (average focusing efficiency ≈55%), and preserve polarization insensitivity. In addition, the holographic design concept provides a new and general method for achromatic metalens in multiple spectra. These highlights are manifested clearly in Table S1 (Supporting Information),

which sums up the representative breakthroughs with seven key parameters: manufacture, spectrum range, polarization response, aperture, efficiency, number of layers, and materials.

2. Results and Discussion

2.1. Concept of the Randomly Interleaved Holographic Broadband Metalens

Figure 1 illustrates the construction process of a randomly interleaved diffractive lens to achieve broadband performance within a shared aperture. As shown in (i) of Figure 1a, the phase distributions of Fresnel diffractive lenses are designed with the same focal length for different wavelengths. The spatially hyperbolic phase profile φ_i of each Fresnel diffractive lens is given by

$$\varphi_i(r) = \frac{2\pi}{\lambda_i}\left(f - \sqrt{r^2 + f^2}\right) \tag{1}$$

where f is the focal length and r is the radial coordinate. λ_{min}, λ_{middle}, λ_{max} correspond to Fresnel diffractive lenses designed for monochromatic illumination at 400, 590, and 750 nm, respectively, which are referred to as the blue (B), green (G), and red (R) channels. The three channels show dramatic chromatic focal dependence, as shown by the ray tracing in Figure 1b. Fresnel diffractive lens operates by means of interference of light transmitted through a phase mask, where the dispersion characteristic
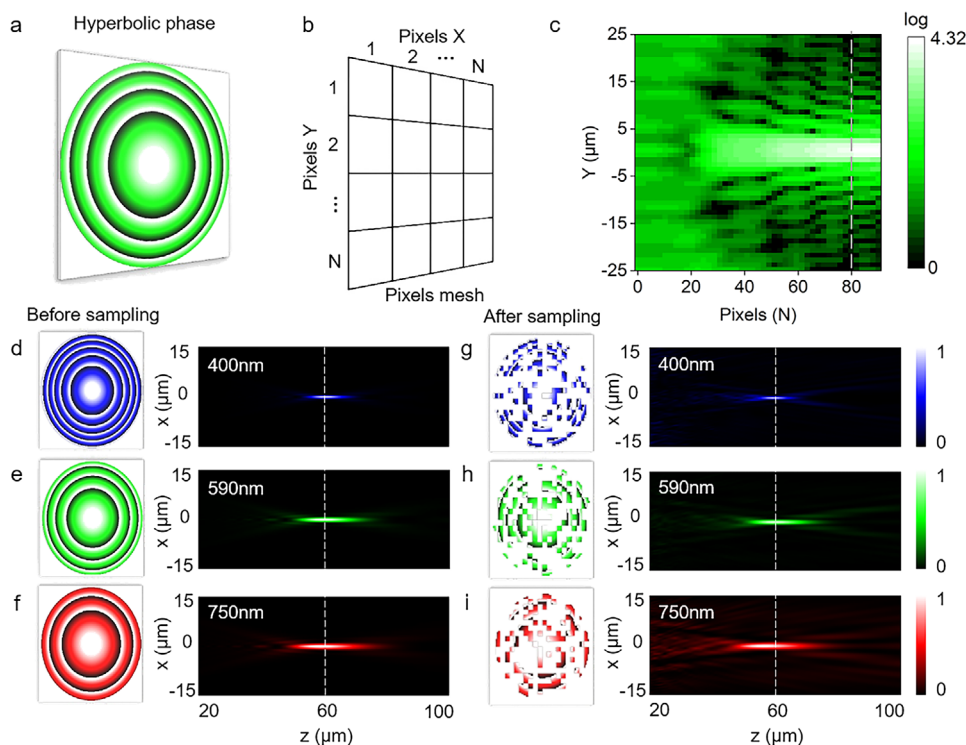
**ADVANCED
SCIENCE NEWS**

www.advancedsciencenews.com

LASER
& PHOTONICS
REVIEWS

www.lpr-journal.org

Figure 2. Numerical simulation of the holographic achromatic metalens. a) Hyperbolic phase distribution at the wavelength of 590 nm. b) Sampling mesh of the entire diffractive surface. c) The light intensity along the y direction of the focal plane as a function of the number of pixels in the diffraction plane. The gray dashed line indicates the number of selected pixels $N = 80$. d–f) The optical field distribution for hyperbolic phases at operating wavelengths of 400 nm (d), 590 nm (e), and 750 nm (f), respectively. g–i) The corresponding optical field at operating wavelengths of 400 nm (g), 590 nm (h), and 750 nm (i) after random sampling.

is inversely proportional to the focal length, that is, the larger the wavelength, the smaller the focal length. In order to balance the PSF of the diffractive lens at multiple wavelengths, we employ a multiplexing approach to generate a three-channel diffraction hologram. In (ii) of Figure 1a, the random sampling is shown in which the subapertures have sizes of $N \times N$ pixels, and the three probabilities are equal ($p_B = p_G = p_R$). Additionally, we can change the weight of each channel by varying the probabilities (p_B, p_G, p_R) with $p_B + p_G + p_R = 1$. These pixels fit together to form a single, multiwavelength holographic lens that fills the entire surface area, as shown in (iii) of Figure 1a. The randomly interleaved holographic lens exhibits wavelength-independent focusing characteristics (Figure 1c). It is worth mentioning that the chromaticity of the RIL focus can be determined by the probabilities of the RGB channels. Meanwhile, the randomly interleaved multiplexing of a single pixel can make the pixel distribution more uniform to decrease the sidelobe in the focusing plane caused by conventional ring multiplexing.[51]

2.2. Principle and Design of the Randomly Interleaved Holographic Broadband Metalens

The number of pixels (N) of the diffraction aperture determines the focusing performance of the holographic metalens. As a proof of the concept, we selected channel G for meshing (**Figure 2**a,b). The focal intensity distribution along the y di-

rection was different after meshing with different N values, as shown in Figure 2c. As the number of pixels increased, the focus got close to the diffraction limit. Weighing the focusing ability against sample fabrication, $N = 80$ (gray dashed line) was chosen as the number of pixels of the diffraction aperture for random sampling. Subsequently, by presetting the focal length $f = 60$ μm for the hyperbolic phases of RGB channels, the axial light field of each channel was numerically calculated (Figure 2d–f). In terms of random sampling, changing the probabilities of the three channels to $p_B : p_G : p_R = 1{:}1.5{:}1$, the axial light fields of the three sets of sampled subapertures were shown in Figure 2g–i. The focal positions were basically unchanged after sampling due to the property that the partial hologram can reproduce the whole information. Taking the three sets of subapertures together, we obtained the phase profile of the holographic metalens. The PSF of the randomly interleaved holographic metalens with the sampling ratio of 1:1.5:1 can be balanced in a certain wavelength range (Figure S1, Supporting Information). In addition, the chromaticity of the metalens can be adjusted by changing the sampling ratio (Figure S2, Supporting Information).

We consider constructing a square polymer column with a low refractive index ($n = 1.5$) of wide W and height H as the artificial neuron phase unit, arranged in a $L \times L$ square lattice. Each lattice operates as an element where its effective refractive index, $n_{eff}(W)$, can be modified by adjusting the square polymer column width W. When a square polymer column fills the entire unit cell ($W = L$), the effective refractive index attains its maximum

value equal to the bulk refractive index n, as shown in the inset of Figure 1c. The relationship between the transmitted light field and the incident light field is expressed according to Equation (2):

$$\vec{E_t} = n_{eff} \, H \vec{E_{in}} \tag{2}$$

and light traveling through an artificial phase unit accumulates a phase shift φ

$$\varphi = \frac{2\pi n_{eff} H}{\lambda} \tag{3}$$

Thus, the phase shift difference $\Delta\varphi$ between the artificial phase units is given by

$$\Delta\varphi = 2\pi \frac{\Delta H \left(n_{eff} - 1 \right)}{\lambda} \tag{4}$$

We fixed the width ($W = 400$ nm) of the artificial neuron phase unit and changed the height H to achieve the desired phase profiles, where the maximum height modulation corresponded to a phase delay of 2π—one of the basic principles of diffractive optics. Considering the effects of interactions between neuronal units on light field modulation, we numerically simulated the phase shift and transmission amplitude as a function of height in visible light with periodic boundary conditions based on the commercial finite-difference time-domain algorithm, respectively (Figure S3, Supporting Information). The transmittance of the artificial neuron unit in the visible light spectrum was more than 92%, which indicated that the transmission loss of the polymer material to the incident light is low. In terms of phase shift, the phase shifts of the three channels used for designing the RIL almost covered 0–2π, respectively, which satisfied Equation (3). Furthermore, increasing the height of the polymer artificial phase unit can extend it to the near-infrared spectrum, which verifies the universality in multiple spectra of the proposed design principle (Figure S4, Supporting Information). It is worth noting that the loss of materials and size limitation of typical achromatic metalenses make it difficult to expand to multiple spectral ranges.

After completing the mapping between the geometric dimension and the phase shift of the artificial phase unit, we can transform the phase profiles of the three channels into geometric height (Figure S5, Supporting Information). According to Equation (1) and (4), the height ranges corresponding to the three channels were rounded as 0–800, 0–1200, and 0–1500 nm. Subsequently, the height modules of the three channels were randomly interleaved in the same aperture to form the height profiles of the RIL as shown in Figure S5 (Supporting Information). Additionally, each pixel of the height profiles corresponds to an artificial phase unit with the width $W = 400$ nm.

2.3. Fabrication and Characterization of the Randomly Interleaved Holographic Broadband Metalens

The RIL was fabricated by femtosecond laser layer-by-layer writing, and the in-layer fabrication process was controlled by an XY scanning unit while the step between two layers was realized by a nano-positioning stage (Figure S6, Supporting Information). The

optimal fabrication parameter was 5.9 mW laser power at 1 ms exposure time, and the point spacing in the x and y directions was 200 nm (Figure S7, Supporting Information). **Figure 3**a illustrates scanning electron microscope (SEM) images of the proposed randomly interleaved diffractive lens with a diameter of 32 μm. To improve the adhesion force of the structure to the silica substrate and avoid the destruction of the integrity of the structure during the development process, a polymer disk with a diameter of 38 μm and a thickness of 200 nm was fabricated at the bottom of the lens. The presence of the isotropic disk does not affect the phase modulation of the lens. In addition, the magnified area image in the inset of Figure 3a shows that the width W of the fabricated phase unit is 409–454 nm, slightly larger than the design size. It is worth mentioning that the manufacturing error of the artificial unit has little effect on the modulation of the light field, as shown in Figure S8 (Supporting Information). As can be seen from the local 3D atomic force microscope (AFM) images (Figure 3b), a small tapering angle can be observed in our fabricated square polymer columns due to the ellipsoid shape of the diffraction-limited focal voxel. The fundamental building block in 3D laser printing, however, in terms of amplitude and phase modulation, the discrepancy between square polymer columns with a straight and tapered top is small.[41] Moreover, the RIL topography extracted along the black dashed part of the local 3D AFM profile shows consistency with the designed contour (Figure 3c). The appearance of non-step-like smooth transitions is due to the self-smoothing effect[52] as shown in the inset in Figure 3c.

To characterize the broadband focusing performance of RIL, Figure 3d plots cross sections of optical intensity in a plane containing the optical axis for each wavelength. The measured axial focal positions of the randomly interleaved diffractive lens remain close to identical ($z = 57$ μm) for different wavelengths, verifying that our RIL is achromatic in nature. The measured focal length coincides with the position of the PSF equilibrium point at each discrete wavelength in the numerical calculation (Figure S1, Supporting Information). As a contrast, we measured the axial light field of a Fresnel lens with the same aperture, and its focal length exhibits a wavelength-dependent property (Figure S9, Supporting Information). It is worth noting that in principle the multiplexed achromatic metalens must produce various monochromatic focalizations. However, due to the equal focal length programmed in the three Fresnel hyperbolic phase channels and the appropriate random sampling probabilities set in the design stage, the focal length at the illumination wavelength is much more efficient and coincides in the same plane, which is the focus plane of interest for us. While remaining monochromatic focalizations are less efficient and appear as the noise background, which does not degrade the experimental results obtained as shown in Figure 3d. We defined the focal plane as the z-coordinate of the maximum measured power intensity on top of the RIL, and experimentally characterized the focusing efficiency of our randomly interleaved broadband diffractive lens, giving rise to efficiency values of 54.7%, 46.9%, 52.9%, 63.7%, 52.6%, 50%, and 48% for incident wavelengths of 470, 510, 550, 590, 632, 660, and 690 nm, respectively (Figure 3e). The focusing efficiency is defined as the ratio of integrated power within the circle having a radius of 1.5×full-width at half-maximum (FWHM) to the incident power on the RIL as shown in the inset in Figure 3e.
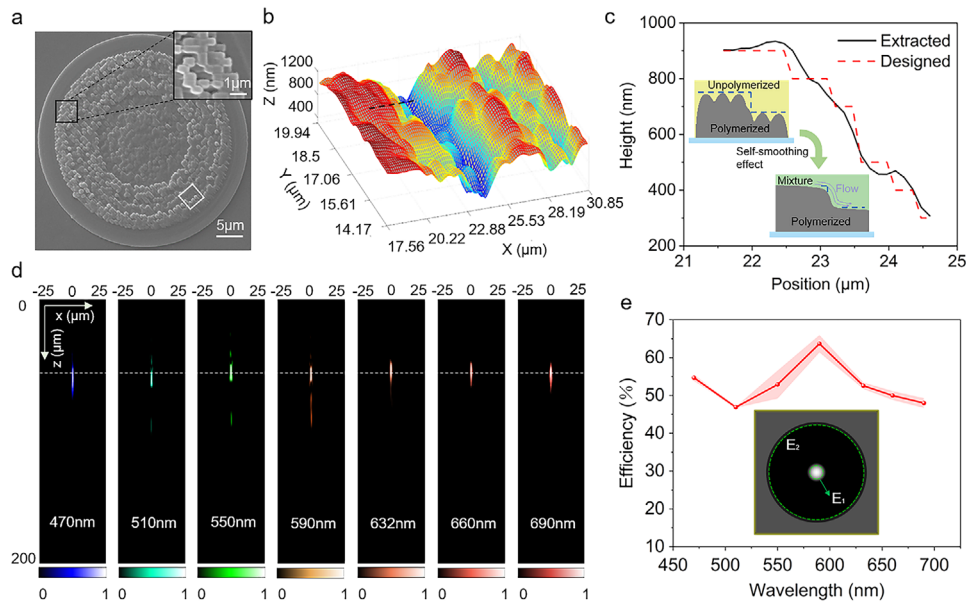
Figure 3. Experimental characterization of the randomly interleaved holographic achromatic metalens. a) SEM of a randomly interleaved diffractive lens. b) 3D local AFM profile of the manufactured RIL, which corresponds to the solid white box in (a). c) Height profiles of the extracted and designed RIL along the black dashed lines in (b). d) Measured longitudinal focal spot intensity at different operating wavelengths. e) Experimentally characterized focusing efficiency of the randomly interleaved diffractive lens at different wavelengths. The lower inset shows the computational model for the focusing efficiency. E_1 represents the energy intensity integral within a radius of 1.5×FWHM of the focused spot. E_2 represents the integral of the energy intensity incident on the device, which is obtained by multiplying the device area with the incident light energy intensity per unit area outside the device at the $z = 0$ plane.

Figure 4a plots cross-sections of the optical power intensity in the focal plane for each wavelength. In Figure 4b, we compare the normalized power intensity distribution of the measured and airy disk at the black dashed in Figure 4a. Obviously, the RIL exhibits a nearly diffraction-limited PSF at multiple discrete wavelengths, and this is quantified in Figure 4c which compares the measured and diffraction-limited ($\frac{0.514\lambda}{NA}$) FWHM for the RIL. Otherwise, to compare the achromatic performance of RIL with that of a single wavelength Fresnel diffractive lens, we define the focusing error as the normalized difference between the nominal and the measured focal length. As shown in Figure 4d, the maximum deviation from the mean focal length of the RIL is measured as 5.26%, while the Fresnel diffractive lens is 15%. This implies that the RIL has effectively corrected chromatic aberration over the entire visible spectrum.

2.4. Imaging Performance of the Randomly Interleaved Holographic Broadband Metalens

The measurement configuration for this imaging demonstration is shown in **Figure 5**a. A white-light LED source was collimated to illuminate the mask after passing through a convex lens and iris, and a series of narrow-band filters with different center wavelengths were placed between the iris and the mask. Then, the image of the object mask illuminated by the polychromatic light was captured by the microscopy system. In the experiments, we adjusted the light path system to make the image clear and then changed only the narrowband filter to another filter or removed it entirely to observe the imaging qualities for light of different col-

ors. Here, we characterized the RIL by imaging the letter "T," and images of different colors on the same focal plane are shown in Figure 5b. In addition, imaging simulations were performed by diffraction tracing, as shown in the inset in the lower-left corner of Figure 5b. The images taken with the RIL exhibited relatively clear line features, showing that the chromatic aberration was improved. In addition, we showed broadband imaging of onion epidermal cells, which held potential applications in biology (Figure S10, Supporting Information). The 1951 United States Air Force (USAF) resolution test chart was used as the imaging target and was imaged with a 5× objective lens under broadband white light illumination. It was obvious that the image of a system without dispersion correction appeared blurred due to the effect of chromatic aberration (Figure 5c). Meanwhile, we compared the imaging of the Fresnel diffractive lens and RIL with the same aperture under white light illumination. The image quality of the Fresnel lens decreased due to chromatic aberration, while RIL effectively improved the situation (Figure S11, Supporting Information). In terms of resolution, (i) of Figure 5d showed that an image of the pattern in the red dashed box of Figure 5c captured by the RIL with white light illumination, and the intensity curve was plotted along the red dashed line in (ii) of Figure 5d. It is worth mentioning that the resolution of the image of 32 μm diameter RIL is up to 0.92 μm, which is consistent with the measured FWHM.

Integral imaging (light-field cameras), one of the most promising 3D imaging techniques, was first proposed by Gabriel Lippmann in 1908.[53] As a common component for integrated imaging, the performance and production of microlens arrays have limited the development of light-field cameras.[54] Here, we demonstrated the broadband imaging of achromatic microlens
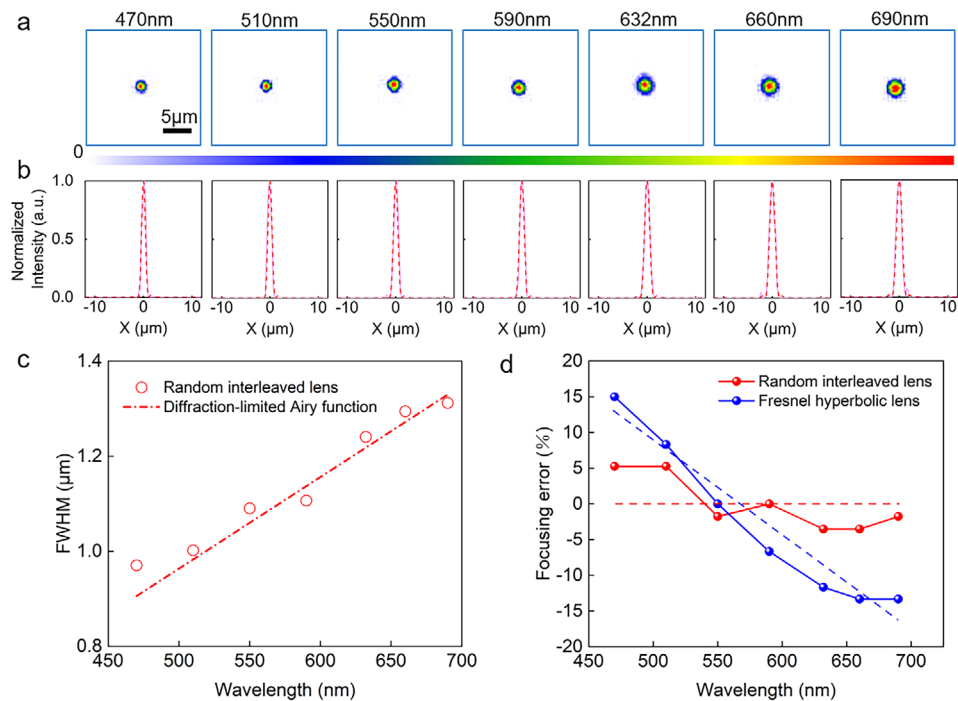
Figure 4. Experimental characterization of the point spread function of the randomly interleaved holographic achromatic metalens. a) Power intensity distribution in the x–y focal plane at different wavelengths. Maximum power intensity appears around the focal plane at $z = 57$ μm. b) Comparison of the diffraction-limited Airy function (dashed red curve) and the measured power intensity across the focal plane (solid blue curve). c) Comparison of the measured FWHM with the diffraction limit. Dashed lines represent diffraction-limited performance. d) Focal length error versus wavelength of the random interleaved lens and the Fresnel lens.

arrays. The microlens array consisted of 2×4 random iterative holographic broadband metalenses and showed the capability of broadband achromatic imaging (Figure S12, Supporting Information). More importantly, thanks to the high efficiency of femtosecond laser two-photon lithography, the manufacturing time of a single achromatic metalens was only 8 minutes, which greatly reduced the time cost for large-scale manufacturing of full-color light-field cameras.

3. Conclusion

In summary, we have demonstrated a holographic metalens that enables broadband achromatic imaging, achieved by randomly interleaving the sub-aperture of three different channels (RGB), with the weight of sampling each channel determining the chromaticity of the diffractive lens focus. As an experimental demonstration, the low-index polymer square column was used as the artificial neuron phase unit, and we fabricated a randomly interleaved broadband diffractive lens with a diameter $D = 32$ μm using the femtosecond laser layer-by-layer scanning strategy. Evaluating the performance of the lens, we found that the focal length of the multiple discrete wavelengths was almost the same (focus deviation is 5.26%), and the average focusing efficiency of the multiple wavelengths was approximately 55%. Furthermore, the imaging experiment showed that the lines of the patterns imaged by the diffractive lens at multiple wavelengths were clear, which proved that the diffractive lens reduced the influence of chromatic aberration on the imaging quality. In addition, the imag-

ing resolution was 0.92 μm. Compared with most metalenses, we have achieved high performance with low refractive index materials, allowing large-scale replication of the structure at low cost, which is beneficial to the development of light field cameras[55] and holds great promise in optoelectronic integration[56,57] and endoscopic imaging.[58] Although we have only experimentally verified the broadband performance of RIL in the visible spectrum, this design method is indeed a general approach that could be extended to other spectral ranges.

4. Experimental Section

Numerical Simulation: The phase shift and transmission amplitude of the artificial phase unit were calculated on a commercial finite difference time-domain-based software (FDTD Solutions, Lumerical Solutions, Inc., CAN). In the simulation, a plane wave light source was placed inside the substrate and 2 μm below the artificial neuron unit, and a frequency domain field and power monitor was placed 12 μm above the artificial neuron unit to collect transmitted power, and the phase shift was collected at the center point of the monitor. The size of monitor is the 2×2 μm. The commercial mathematical software (MATLAB, MathWorks, US) was used to perform imaging and the point spread function simulation.

Randomly Interleaved Holographic Broadband Metalens Preparation and Characterization: The type of photoresist used for fabricating the randomly interleaved achromatic lens was commercial zirconium–silicon hybrid sol–gel material (SZ2080, IESL-FORTH, Greece). 6 μL of photoresist was pipetted onto the coverslip, then pre-baked it at 100 °C for 45 min to evaporate the solvent in the material, and finally used the direct laser writing to write the designed achromatic microlens inside the photoresist
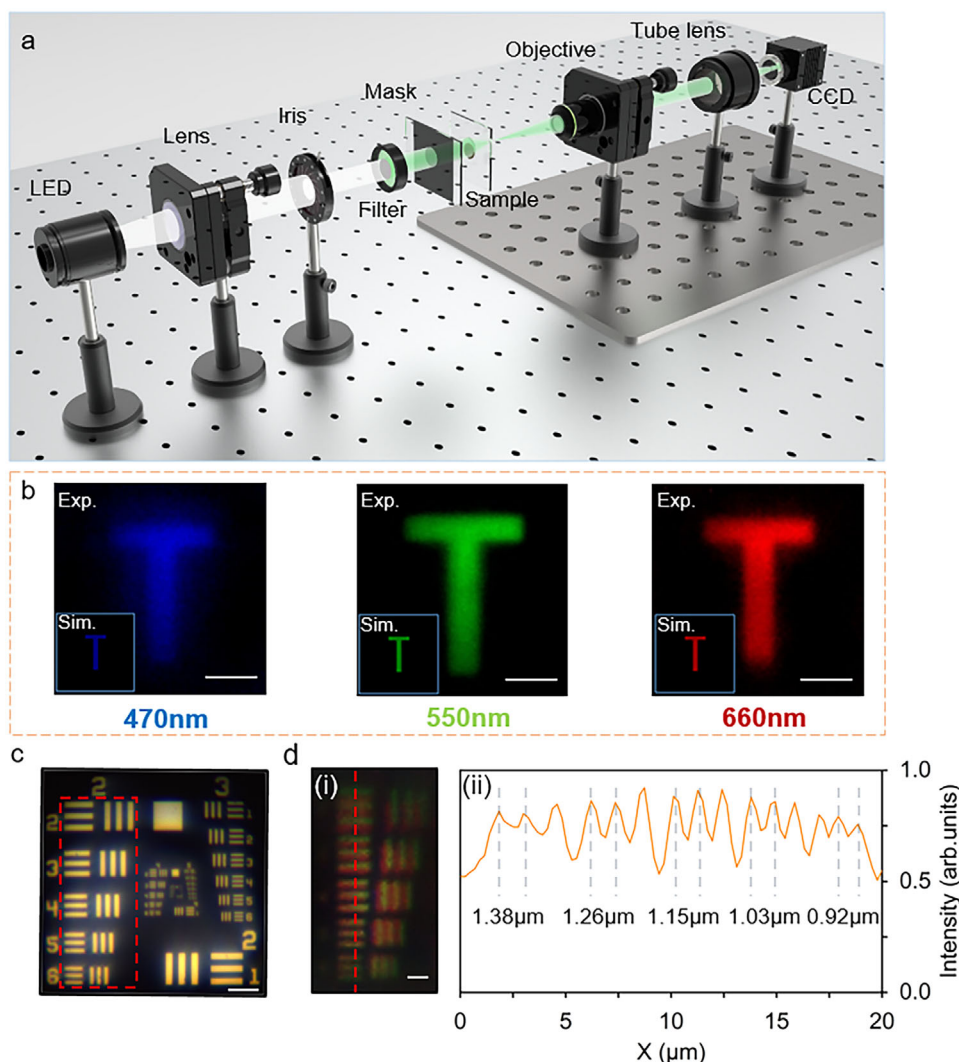
Figure 5. Imaging performance of the randomly interleaved holographic achromatic metalens. a) Measurement configuration for the imaging demonstration of the randomly interleaved diffractive lens. b) Experimental and simulation of imaging results of the letter "T" under the irradiation of 470, 550, and 660 nm wavelengths. c) Captured USAF target image with a 5× objective lens under broadband white light illumination. d) Resolution test results for RIL with a diameter of 32 μm under broadband white light illumination. i) Image result for normal incidence of the red dashed box in (c). ii) Normalized intensity along the red dashed line in (i). The images have a yellowish tint because a warm white LED was used as the illumination. The scale bars are 5 μm in (b), 100 μm in (c), and 2 μm in (d).

material. The femtosecond laser source is a mode-locked Ti: Sapphire ultrafine oscillator (Chameleon Vision-S, Coherent, Inc., US.) with a central wavelength of 800 nm, a pulse width of 75 fs, and a repetition rate of 80 MHz, and focuses on the sample through a 60× oil-immersed objective lens (NA = 1.35, Olympus, JPN) for photopolymerization. After finishing processing, the samples were developed in absolute ethanol for 30 min to remove unpolymerized parts. The SEM images were achieved by a secondary-electron scanning electron microscope (EVO18, ZEISS) with an accelerating voltage of 10 keV after depositing ≈10 nm of gold. The topography of the RIL was scanned at a rate of 0.5 Hz in the air in tapping mode with a commercial atomic force microscope (AFM, MFP3D-origin OXFORD) using a Tap300Al-G tapping mode tip.

The Optical Characterization of the Randomly Interleaved Holographic Broadband Metalens: In the experiment, the focusing characteristics of the sample were measured by the microscope. The position of the sample was changed by moving a nanoscale 3D piezoelectric platform (E-727, Physik Instrumente, U.K.) in a predefined axial increment (1 μm), and the

2D image of each increment was collected by using a CCD camera. The sample plane was chosen as the reference plane for z = 0, and the longitudinal intensity distribution of the sample was acquired through a stack of 2D images by commercial mathematical software (MATLAB, MathWorks, U.S.). The light intensity distribution of different wavelengths was obtained by inserting color filters.

Supporting Information

Supporting Information is available from the Wiley Online Library or from the author.

Acknowledgements

Author Contributions

X.W. and S.L. contributed equally to this work. X.W.,S.L., and W.D. proposed the idea and conceived the experiment. X.W.,S.L.,L.X.,Y.C.,Y.T.,Z.Z., and Y.C. performed the experiments. X.W., and S.L. performed the numerical simulations. X.W. wrote the manuscript. S.L., J.N., C.C., C.W., Y.H., J.L., J.C. and D.W. reviewed and revised the manuscript.

Conflict of Interest

The authors declare no conflict of interest.

Data Availability Statement

The data that support the findings of this study are available from the corresponding author upon reasonable request.

Keywords

[1] M. Born, E. Wolf, *7th, Principles of Optics*, Cambridge University Press, Cambridge **1999**.

[2] X. Ou, T. Zeng, Y. Zhang, Y. Jiang, Z. Gong, F. Fan, H. Jia, H. Duan, Y. Hu, *Nano Lett.* **2022**, *22*, 10049.

[3] A. Miks, J. Novak, *Appl. Optics* **2014**, *53*, 6930.

[4] E. J. Fernandez, P. Artal, *Biomed. Opt. Express* **2017**, *8*, 2396.

[5] T. Stone, N. George, *Appl. Optics* **1988**, *27*, 2960.

[6] R. Sawant, D. Andrén, R. J. Martins, S. Khadir, R. Verre, M. Käll, P. Genevet, *Optica* **2021**, *8*, 1405.

[7] A. Kubec, M.-C. Zdora, U. T. Sanli, A. Diaz, J. Vila-Comamala, C. David, *Nat. Commun.* **2022**, *13*, 1305.

[8] R. E. Parks, presented at *Int. Optical Design Conf.*, Vancouver Canada, June, **2006**.

[9] R. Zhu, J. Wang, T. Qiu, Y. Han, X. Fu, Y. Shi, X. Liu, T. Liu, Z. Zhang, Z. Chu, C.-W. Qiu, S. Qu, *eLight* **2022**, *2*, 10.

[10] Y. Ni, C. Chen, S. Wen, X. Xue, L. Sun, Y. Yang, *eLight* **2022**, *2*, 23.

[11] L. Li, H. Zhao, C. Liu, L. Li, T. J. Cui, *eLight* **2022**, *2*, 7.

[12] E. Tseng, S. Colburn, J. Whitehead, L. Huang, S.-H. Baek, A. Majumdar, F. Heide, *Nat. Commun.* **2021**, *12*, 6493.

[13] S. Wei, G. Cao, H. Lin, X. Yuan, M. Somekh, B. Jia, *ACS Nano* **2021**, *15*, 4769.

[14] R. Wang, M. A. Ansari, H. Ahmed, Y. Li, W. Cai, Y. Liu, S. Li, J. Liu, L. Li, X. Chen, *Light: Sci. Appl.* **2023**, *12*, 103.

[15] M. Liu, W. Zhu, P. Huo, L. Feng, M. Song, C. Zhang, L. Chen, H. J. Lezec, Y. Lu, A. Agrawal, T. Xu, *Light: Sci. Appl.* **2021**, *10*, 107.

[16] M. Pan, Y. Fu, M. Zheng, H. Chen, Y. Zang, H. Duan, Q. Li, M. Qiu, Y. Hu, *Light: Sci. Appl.* **2022**, *11*, 195.

[17] W. T. Chen, A. Y. Zhu, F. Capasso, *Nat. Rev. Mater.* **2020**, *5*, 604.

[18] S. Wang, P. C. Wu, V.-C. Su, Y.-C. Lai, M.-K. Chen, H. Y. Kuo, B. H. Chen, Y. H. Chen, T.-T. Huang, J.-H. Wang, R.-M. Lin, C.-H. Kuan, T. Li, Z. Wang, S. Zhu, D. P. Tsai, *Nat. Nanotechnol.* **2018**, *13*, 227.

[19] S. Wang, P. C. Wu, V.-C. Su, Y.-C. Lai, C. Hung Chu, J.-W. Chen, S.-H. Lu, J. Chen, B. Xu, C.-H. Kuan, T. Li, S. Zhu, D. P. Tsai, *Nat. Commun.* **2017**, *8*, 187.

[20] W. T. Chen, A. Y. Zhu, V. Sanjeev, M. Khorasaninejad, Z. Shi, E. Lee, F. Capasso, *Nat. Nanotechnol.* **2018**, *13*, 220.

[21] Y. Wang, Q. Chen, W. Yang, Z. Ji, L. Jin, X. Ma, Q. Song, A. Boltasseva, J. Han, V. M. Shalaev, S. Xiao, *Nat. Commun.* **2021**, *12*, 5560.

[22] J. Engelberg, U. Levy, *Nat. Commun.* **2020**, *11*, 1991.

[23] G. Yoon, K. Kim, S.-U. Kim, S. Han, H. Lee, J. Rho, *ACS Nano* **2021**, *15*, 698.

[24] R. C. Devlin, M. Khorasaninejad, W. T. Chen, J. Oh, F. Capasso, *Proc. Natl. Acad. Sci. USA* **2016**, *113*, 10473.

[25] M. Horák, K. Bukvisová, V. Svarc, J. Jaskowiec, V. Křápek, T. Sikola, *Sci. Rep.* **2018**, *8*, 9640.

[26] D. Lee, S. So, G. Hu, M. Kim, T. Badloe, H. Cho, J. Kim, H. Kim, C.-W. Qiu, J. Rho, *eLight* **2022**, *2*, 1.

[27] K. Ou, F. Yu, G. Li, W. Wang, J. Chen, A. E. Miroshnichenko, L. Huang, T. Li, Z. Li, X. Chen, W. Lu, *Laser Photon Rev.* **2021**, *15*, 2100020.

[28] Z. Li, R. Pestourie, J.-S. Park, Y.-W. Huang, S. G. Johnson, F. Capasso, *Nat. Commun.* **2022**, *13*, 2409.

[29] S. Larouche, Y.-J. Tsai, T. Tyler, N. M. Jokerst, D. R. Smith, *Nat. Mater.* **2012**, *11*, 450.

[30] L. Huang, X. Chen, H. Mühlenbernd, H. Zhang, S. Chen, B. Bai, Q. Tan, G. Jin, K.-W. Cheah, C.-W. Qiu, J. Li, T. Zentgraf, S. Zhang, *Nat. Commun.* **2013**, *4*, 2808.

[31] Z.-L. Deng, M. Jin, X. Ye, S. Wang, T. Shi, J. Deng, N. Mao, Y. Cao, B.-O. Guan, A. Alù, G. Li, X. Li, *Adv. Funct. Mater.* **2020**, *30*, 1910610.

[32] X. Zhang, D. Tang, L. Zhou, J. Jiao, D. Feng, G. Liang, Y. Guo, *Nanoscale* **2019**, *11*, 20238.

[33] C. M. Soukoulis, M. Wegener, *Nat. Photon.* **2011**, *5*, 523.

[34] M. Malinauskas, A. Zukauskas, V. Purlys, K. Belazaras, A. Momot, D. Paipulas, R. Gadonas, A. Piskarskas, H. Gilbergs, A. Gaidukeviciute, I. Sakellari, M. Farsari, S. Juodkazis, *J. Opt.* **2010**, *12*, 124010.

[35] M. Malinauskas, A. Zukauskas, S. Hasegawa, Y. Hayasaki, V. Mizeikis, R. Buividas, S. Juodkazis, *Light: Sci. Appl.* **2016**, *5*, e16133.

[36] C. Xin, D. Jin, Y. Hu, L. Yang, R. Li, L. Wang, Z. Ren, D. Wang, S. Ji, K. Hu, D. Pan, H. Wu, W. Zhu, Z. Shen, Y. Wang, J. Li, L. Zhang, D. Wu, J. Chu, *ACS Nano* **2021**, *15*, 18048.

[37] M. Malinauskas, M. Farsari, A. Piskarskas, S. Juodkazis, *Phys. Rep.* **2013**, *533*, 1.

[38] S.-H. Park, D.-Y. Yang, K.-S. Lee, *Laser Photonics Rev.* **2009**, *3*, 1.

[39] Z.-Y. Hu, T. Jiang, Z.-N. Tian, L.-G. Niu, J.-W. Mao, Q.-D. Chen, H.-B. Sun, *Laser Photonics Rev.* **2022**, *16*, 2100537.

[40] M. Tan, L. Huang, J. Cao, H. Zhang, S. Zhao, M. Liu, Z. Jia, R. Zhai, H. Liu, *Opt. Express* **2022**, *30*, 24689.

[41] H. Ren, X. Fang, J. Jang, J. Bürger, J. Rho, S. A. Maier, *Nat. Nanotechnol.* **2020**, *15*, 948.

[42] L. Yang, A. El-Tamer, U. Hinze, J. Li, Y. Hu, W. Huang, J. Chu, B. N. Chichkov, *Opt. Laser. Eng.* **2015**, *70*, 26.

[43] L. Zhang, B. Liu, C. Wang, C. Xin, R. Li, D. Wang, L. Xu, S. Fan, J. Zhang, C. Zhang, Y. Hu, J. Li, D. Wu, L. Zhang, J. Chu, *Nano Lett.* **2022**, *22*, 5277.

[44] L. Jonusauskas, S. Rekstyte, M. Malinauskas, *Opt. Eng.* **2014**, *53*, 125102.

[45] F. Balli, M. Sultan, S. K. Lami, J. T. Hastings, *Nat. Commun.* **2020**, *11*, 3892.

[46] F. Balli, M. A. Sultan, A. Ozdemir, J. T. Hastings, *Nanophotonics* **2021**, *10*, 1259.

[47] H. Ren, J. Jang, C. Li, A. Aigner, M. Plidschun, J. Kim, J. Rho, M. A. Schmidt, S. A. Maier, *Nat. Commun.* **2022**, *13*, 4183.

[48] E. Goi, X. Chen, Q. Zhang, B. P. Cumming, S. Schoenhardt, H. Luan, M. Gu, *Light: Sci. Appl.* **2021**, *10*, 40.

[49] D. Veksler, E. Maguid, N. Shitrit, D. Ozeri, V. Kleiner, E. Hasman, *ACS Photonics* **2015**, *2*, 661.

[50] E. Maguid, I. Yulevich, D. Veksler, V. Kleiner, M. L. Brongersma, E. Hasman, *Science* **2016**, *352*, 1202.

[51] A. Márquez, C. Iemmi, J. Campos, M. J. Yzuel, *Opt. Lett.* **2006**, *31*, 392.

[52] K. Takada, H.-B. Sun, S. Kawata, *Appl. Phys. Lett.* **2005**, *86*, 071122.

[53] G. Lippmann, *C. R. Acad. Sci.* **1908**, *146*, 446.

[54] R. J. Lin, V.-C. Su, S. Wang, M. K. Chen, T. L. Chung, Y. H. Chen, H. Y. Kuo, J.-W. Chen, J. Chen, Y.-T. Huang, J.-H. Wang, C. H. Chu, P. C. Wu, T. Li, Z. Wang, S. Zhu, D. P. Tsai, *Nat. Nanotechnol.* **2019**, *14*, 227.

[55] Z.-B. Fan, H.-Y. Qiu, H.-L. Zhang, X.-N. Pang, L.-D. Zhou, L. Liu, H. Ren, Q.-H. Wang, J.-W. Dong, *Light: Sci. Appl.* **2019**, *8*, 67.

[56] Z.-Y. Hu, Y.-L. Zhang, C. Pan, J.-Y. Dou, Z.-Z. Li, Z.-N. Tian, J.-W. Mao, Q.-D. Chen, H.-B. Sun, *Nat. Commun.* **2022**, *13*, 5634.

[57] E. Goi, S. Schoenhardt, M. Gu, *Nat. Commun.* **2022**, *13*, 7531.

[58] J. Li, S. Thiele, B. C. Quirk, R. W. Kirk, J. W. Verjans, E. Akers, C. A. Bursill, S. J. Nicholls, A. M. Herkommer, H. Giessen, R. A. Mclaughlin, *Light: Sci. Appl.* **2020**, *9*, 124.